

# Lawrence Berkeley National Laboratory

## Lawrence Berkeley National Laboratory

### **Title**

Ni implanted ZnO single crystals: Correlation between nanoparticle formation and defect structure

### **Permalink**

<https://escholarship.org/uc/item/54k9n98p>

### **Author**

Arenholz, Elke

### **Publication Date**

2007-10-04

Ni implanted ZnO single crystals – correlation between nanoparticle formation and defect structure

Shengqiang Zhou, K. Potzger, K. Kuepper, J. Grenzer, M. Helm, and J. Fassbender  
Institute of Ion Beam Physics and Materials Research, Forschungszentrum Dresden-Rossendorf, P.O. Box 510119, 01314 Dresden, Germany

E. Arenholz, J. D. Denlinger  
Advanced Light Source, Lawrence Berkeley National Laboratory, Berkeley, California 94720

We show that metallic secondary phase formation inside ZnO(0001) single crystals implant-doped with Ni at an atomic concentration of 5 % can be suppressed. All the Ni ions are in 2<sup>+</sup> valence state after mild post-annealing. The suppression is achieved by means of annealing of the crystals in high vacuum prior to implantation and is correlated with structural defects of the ZnO single crystals. The observed ferromagnetic properties of the pre-annealed crystals degrade at ambient temperature within several days.

## I. Introduction

Ferromagnetic doped and undoped oxides have recently attracted huge attention. Among them, diluted magnetic semiconductors (DMS) with a Curie temperature above room temperature exhibit a high application potential in spintronics<sup>1</sup>. Although a variety of candidates for such material exist, e.g. transition metal (TM) doped ZnO<sup>2-4</sup>, the research community is far from harmony with their results. The main problem appears to be that different sources of ferromagnetism in transition metal doped ZnO like nanoparticles of ferromagnetic secondary phases<sup>5-7</sup> or giant magnetic moments (GMM)<sup>7-13</sup> can mimic a ferromagnetic DMS. Nanophases are usually difficult to detect by means of common structural analysis methods<sup>5</sup> but might lead to magneto-transport properties similar to those expected for DMS<sup>14</sup>. The origin of GMM – on the other hand - is still controversial. De-quenching of orbital moments in isolated atoms<sup>9-10</sup> or doped clusters<sup>11</sup>, coupled orbital states with large radii<sup>13</sup> as well as defect induced ferromagnetism<sup>12</sup> are discussed. Another source of ferromagnetic signals in magnetometry which has to be seriously discussed is unwanted contamination by using steel tools for handling the samples<sup>15</sup>. In ref. 15 the authors systematically investigated the effect of handling different substrates using steel tweezers including HfO<sub>2</sub>. They were able to induce ferromagnetism that easily can be interpreted to be defect induced. As best to our knowledge, systematic investigations of artifacts from common magnetometers are not published so far.

## II. Experiment

The key point of our preparation is the annealing of commercial hydrothermal ZnO(0001) single crystals prior to implantation in high vacuum (base pressure  $< 1 \times 10^{-6}$  mbar) at a temperature of 1323 K for 15 min. The ideas behind this treatment (table I) are

- Avoidance of secondary phase formation after transition metal implantation and post-annealing<sup>16</sup>.
- Creation of defects that can lead to ferromagnetic order.

Double side polished ZnO(0001) is excellently suited, since the Zn-face is less stable under thermal treatment than the O-face. Therefore, the majority of defects is created in a controlled way at the Zn-terminated side. The surface roughness is increased due to the pre-annealing from 0.2 nm up to maximum 116 nm (defined as the root mean square average of the height deviations  $R_q$ ) as was found by atomic force microscopy (not shown). High resolution analysis of the defects introduced into the material due to the preparation is provided later. Ion implantation itself offers a non-equilibrium doping technique suited to achieve the necessary high dopant concentration<sup>18-19</sup>.  $\text{Ni}^+$  implantation was performed at an energy of 80 keV. We used an implantation temperature of 253 K in order to avoid Ni nanoparticle formation already during implantation, an incidence angle of  $7^\circ$ , and a fluence of  $2 \times 10^{16} \text{ cm}^{-2}$  yielding a maximum atomic concentration of 5 % at a depth of 37 nm (straggling of 16 nm). After implantation the sample  $\text{Ni:ZnO}_{\text{vac}}$  was annealed in high vacuum (base pressure  $< 1 \times 10^{-6}$  mbar) at a temperature of 823 K which is suited to activate magnetic coupling in other systems as was reported earlier<sup>20</sup>. For comparison a non pre-annealed, i.e. as purchased crystal ( $\text{Ni:ZnO}_{\text{purch}}$ ) was treated equally. For the latter Ni nanoclusters formation is expected<sup>7</sup>. Moreover, a non-implanted sample ( $\text{XX:ZnO}_{\text{vac}}$ ) which was treated like  $\text{Ni:ZnO}_{\text{vac}}$  was analyzed. In order to prevent ferromagnetic contamination, we have used ceramic tools

for handling. Sample holders for implantation and annealing were made from pure Mo or Cu.

Sample I.D.	Pre-annealing treatment	Implantation and post-implantation treatment
Ni:ZnO <sub>purch</sub>	Non (as purchased)	Implantation plus post-annealing at 823 K for 15 min
Ni:ZnO <sub>vac</sub>	Annealing at 1323 K for 15 min	
XX:ZnO <sub>vac</sub>	Annealing at 1323 K for 15 min	No implantation, annealing at 823 K for 15 min

Table I. Sample nomenclature. All crystals were prepared from the same production charge.

Several analysis techniques have been applied in order to obtain a consistent picture of our systems. The electronic properties were investigated by X-ray absorption spectroscopy (XAS) and X-ray magnetic circular dichroism (XMCD) at the Ni L absorption edge. These experiments were performed at beamline 8.0.1 and 6.3.1 of the Advanced Light Source (ALS) in Berkeley, respectively. Structural properties were investigated by means of X-ray diffraction (XRD) using a Siemens D5005 diffractometer equipped with a Göbel mirror for higher brilliance, and by means of high resolution (HR) XRD using a GE HXRD 3003. Moreover, we performed SQUID magnetometry with magnetic field H applied parallel to the sample surface.

### III. Avoidance of secondary phase formation

To study the formation of metallic secondary phases in the samples Ni:ZnO<sub>purch</sub> and Ni:ZnO<sub>vac</sub>, XAS at the Ni L<sub>2,3</sub> absorption edge was employed, i.e. the Ni charge state was determined. Both total electron yield (TEY) and total fluorescence yield (TFY) were

recorded during the measurement. While TFY is bulk sensitive, TEY probes the surface near region. The valence state of the Ni ions in the as-implanted crystals is mostly  $2^+$  as determined by comparing TEY data (not shown) with those from Ni metal and NiO. This suggests that for low temperature ion implantation metallic secondary phase formation is impeded. However, after annealing there is a significant difference of the XA spectra between Ni:ZnO<sub>purch</sub> and Ni:ZnO<sub>vac</sub> as shown by the two upper spectra in Fig. 1(a). Further analysis of the spectra is performed by qualitative comparison of the XAS of Ni:ZnO<sub>vac</sub> and Ni:ZnO<sub>purch</sub> with the ones of NiO and Ni metal, i.e. the two lower spectra in Fig. 1(a). From those one can conclude that only the post-annealed Ni:ZnO<sub>purch</sub> sample shows pronounced metallic contribution which is in good agreement with the XRD data (see below). On the other hand, the post-annealed Ni:ZnO<sub>vac</sub> shows no contributions from metallic Ni. Here all the implanted Ni ions exhibit a  $2^+$  valence state. Note that, apparently, there is a difference between the spectra for NiO and for Ni:ZnO<sub>vac</sub> (Fig. 1a). [Question: Where those samples measured that the same beamline. The energy resolution appears to be different.]The reason for these deviations might be a different crystal field strength or environment which changes the multiplet structure of the Ni L<sub>2,3</sub> absorption edges. From Fig. 1a-b it is evident, that the spectra of both TEY and TFY mode are in good agreement for the post-annealed crystals. Hence we conclude that there is no difference between the bulk and near surface charge distribution.

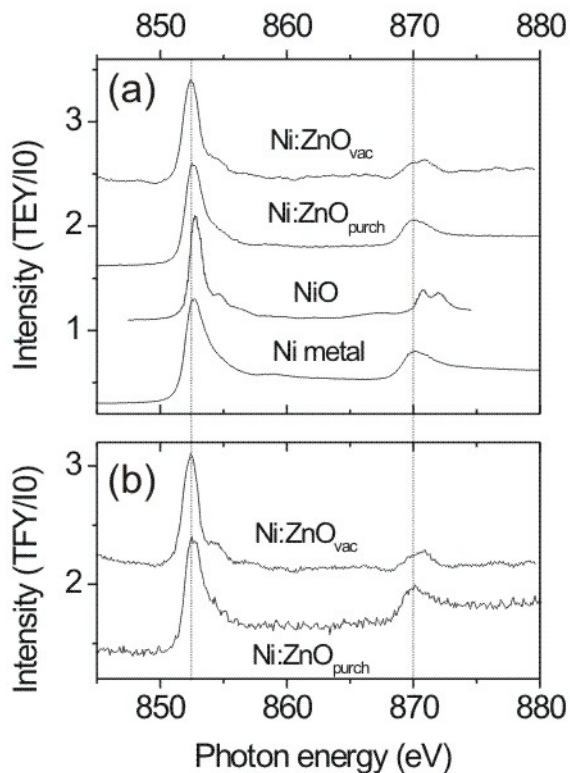


Fig. 1(a). XA spectra of post-annealed Ni:ZnO<sub>vac</sub> and Ni:ZnO<sub>purch</sub> (upper two spectra) in comparison with NiO<sup>21</sup> and metallic Ni (lower two spectra) measured in TEY detection mode. (b) TFY spectra of post-annealed Ni:ZnO<sub>vac</sub> and Ni:ZnO<sub>purch</sub>. All spectra have been y-shifted for better visibility.

Aiming at the structural investigation/exclusion of secondary phases in post-annealed Ni:ZnO<sub>purch</sub> and Ni:ZnO<sub>vac</sub>, Bragg-Brentano angular scans by means of XRD have been performed. Crystalline Ni nanoparticles are only found in post-annealed Ni:ZnO<sub>purch</sub> (Fig. 2). Their mean diameter is determined to 7 nm by using the Scherrer formula<sup>23</sup>. Their uniform alignment with respect to the ZnO crystal lattice has been explained in detail previously<sup>7</sup>. It is worth to note that due to such fixed epitaxial relation it is possible to detect nanoparticles by using lab XRD setups in contrast to, e.g., randomly aligned Fe

nanoparticles that can be detected only with synchrotron XRD<sup>5</sup>[a comment on why would be necessary here]. For post-annealed Ni:ZnO<sub>vac</sub> no crystalline secondary phases have been detected.

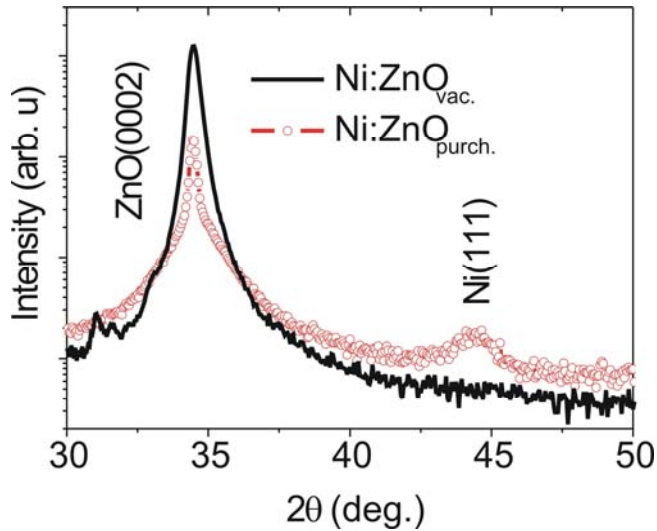


Fig. 2. XRD 2θ-θ scans for Ni implanted ZnO after post annealing. Ni nanoparticles are only detectable in the sample of ZnO<sub>purch.</sub>

In summary we have demonstrated that Ni can be incorporated into pre-annealed ZnO single crystals by means of ion implantation and post-annealing without secondary phase formation.

#### IV. Correlation between structure and magnetic properties

For the characterization of the crystal defect structure high resolution (HR) reciprocal space mapping (RSM) using HR-XRD was performed. The evolution of the lattice disorder, for XX:ZnO<sub>vac</sub>, Ni:ZnO<sub>vac</sub> and Ni:ZnO<sub>purch.</sub>, induced by the preparation steps as compared to a virgin crystal from the same charge is shown in Fig. 3a. The analysed

ZnO crystals, especially  $XX:ZnO_{vac}$  and  $Ni:ZnO_{vac}$ , show a mosaic crystal structure, i.e. a microtexture, after thermal treatment and implantation. This can be understood in the following way: The crystal is broken into a large number of perfect grains slightly disoriented one from the other and separated by dislocation walls (grain boundaries). The FWHM given in Figure 3a describes the angular distribution of these disoriented grains.  $Ni:ZnO_{purch}$  shows roughly constant mosaicity along with the preparation. Even a small decrease of the mosaicity can be observed after post-annealing indicating lattice recovery. For  $Ni:ZnO_{purch}$ , the tensile strain drastically increases with implantation and decreases slightly after post annealing. A clear increase of mosaicity and tensile strain is, however, observed for pre-annealed  $XX:ZnO_{vac}$  or  $Ni:ZnO_{vac}$ . Exemplarily, the lattice defect structure for a virgin sample before and after pre annealing (Fig. 3 b-c) as well as for  $Ni:ZnO_{purch}$  and  $Ni:ZnO_{vac}$  for different preparation steps (Fig. 3 d-g) are shown. The increase of the tensile strain component for  $Ni:ZnO_{vac}$  may be directly attributed to the strained regions, i.e. grain boundaries.

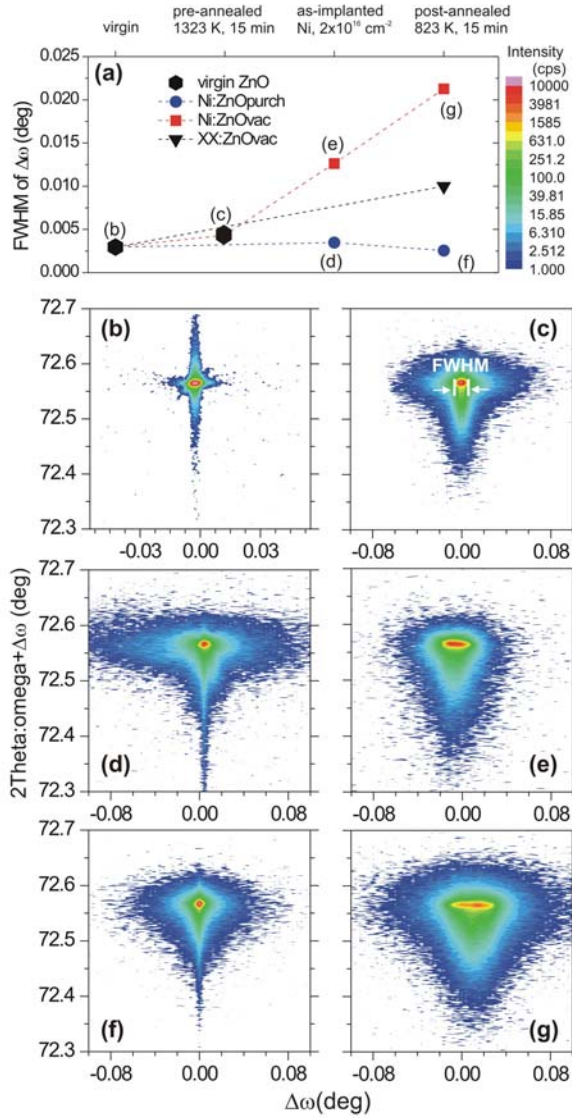


Fig. 3. Results from RSM of the (004) symmetrical reflection. (a) represents the evolution of the FWHM reflecting the crystal mosaicity along with the preparation steps indicated on the upper x-axis. (b)-(g) show RSM for selected data points of (a). With pre-annealing the crystal mosaicity increases (c) in comparison to the virgin sample (b). For those crystals the mosaicity also increases along with further preparation (e-g). It stays, however, nearly constant for Ni:ZnO<sub>purch</sub> (b-f).

In order to relate the structural to magnetic properties, SQUID magnetometry has been performed. The virgin samples are purely diamagnetic. Applying a zero field cooling / field cooling (ZFC/FC) protocol a behavior representative for superparamagnetic nanoparticle systems was only found for the post-annealed Ni:ZnO<sub>purch</sub> (Fig. 4a). Here the magnetization vs. temperature curves were obtained during heating and subsequently cooling the sample in a field of 50 Oe after cooling it down from 300 K to 5 K in zero field, A maximum magnetization at  $T_{max}$ , close to the superparamagnetic deblocking temperature is clearly visible. The broad shape of the peak suggests also a broad size distribution of the nanoparticles. The coercivity  $H_C$  and saturation magnetization  $M_S$  decay fast with increasing temperature, i.e. from  $H_C=467$  Oe and  $M_S=0.15 \mu_B$  at 5 K down to  $H_C\sim 0$  and  $M_S=0.07 \mu_B$  at 300 K. Concordantly, XMCD (TEY) at the Ni absorption edge (Fig. 4b) revealed a pronounced dichroic behavior under magnetization reversal again only for Ni:ZnO<sub>purch</sub>. Note that - in agreement with the XAS data - the ferromagnetic properties for Ni:ZnO<sub>purch</sub> solely stem from metallic Ni, so that there is also no “hidden” contribution from DMS. Thus, figure 4b shows the XA- and XMCD-spectra for the circularly polarized incident radiation. Applying a longitudinal external magnetic field of  $H = \pm 0.2$  T the intensity distribution of the spectra differs for both field directions. The sample magnetization has been flipped at any point recorded. The difference in fluorescence yield is displayed by the asymmetry ratio  $I_{XMCD}(E) = (I_+ - I_-) / (I_+ + I_-)$ . We found an asymmetry of about 10% at the Ni  $L_3$  edge. The overall shape and magnitude of XMCD is similar to that found for Ni metal<sup>24</sup>.

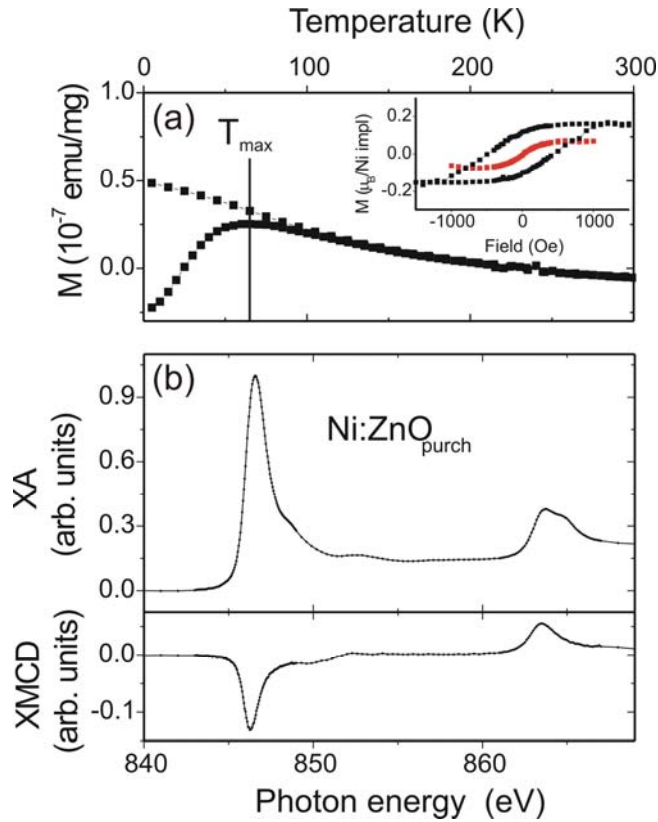


Fig. 4. (a) SQUID ZFC/FC temperature dependence recorded at 50 Oe and magnetization reversal (insets) measured at 5 K and 300 K, respectively, for Ni:ZnO<sub>purch</sub>. The magnetization is given either with respect to the ZnO sample (emu/mg) or to the total number of Ni ions implanted ( $\mu_B/\text{Ni impl}$ ). The diamagnetic background from ZnO was subtracted for the inset. (b) XMCD of Ni:ZnO<sub>purch</sub> after post-annealing. The spectrum was recorded at 15 K and 30° grazing incidence with fields of  $H=\pm 0.2$  T using TEY. The upper represent the total X-ray absorption (XA), i.e. the sum of the XA spectra for both circular polarizations of the X-rays, and thus corresponds to the spectrum for Ni:ZnO<sub>purch</sub> in fig. 1a. The lower represents the x-ray magnetic dichroism (XMCD).

For the vacuum pre-annealed crystals after post-annealing, ferromagnetic ordering, i.e. differences between ZFC and FC temperature dependence as well as hysteresis loops upon magnetization reversal have been found (Fig. 5a). Magnetometry was performed

24 h subsequently to the thermal treatment. A weak ferromagnetic background about  $2 \times 10^{-8}$  emu/mg of unknown origin as well as a weak separation of the ZFC/FC curve are observed for XX:ZnO<sub>vac</sub> (not shown). If the hysteresis loop is scaled like the ones for Ni:ZnO<sub>vac</sub> (Fig. 5 a), i.e. with respect to the amount of  $2 \times 10^{16}$  cm<sup>-2</sup> implanted Ni, the saturation magnetization for XX:ZnO<sub>vac</sub> only amounts to 0.03  $\mu_B$  “per implanted Ni ion”. For Ni:ZnO<sub>vac</sub>,  $M_S$  is considerably larger than for XX:ZnO<sub>vac</sub>. It amounts to 0.1  $\mu_B$  per implanted Ni ion. After 3 days the saturation magnetization is lowered to a value comparable to the one of XX:ZnO<sub>vac</sub> with a stability on a scale of two months at ambient temperatures. XMCD at the Ni L-edge for Ni:ZnO<sub>vac</sub> performed 4 weeks after post-annealing did not yield clear magnetic ordering (Fig. 5b). The latter can, however, be attributed to the low saturation magnetization after degradation.

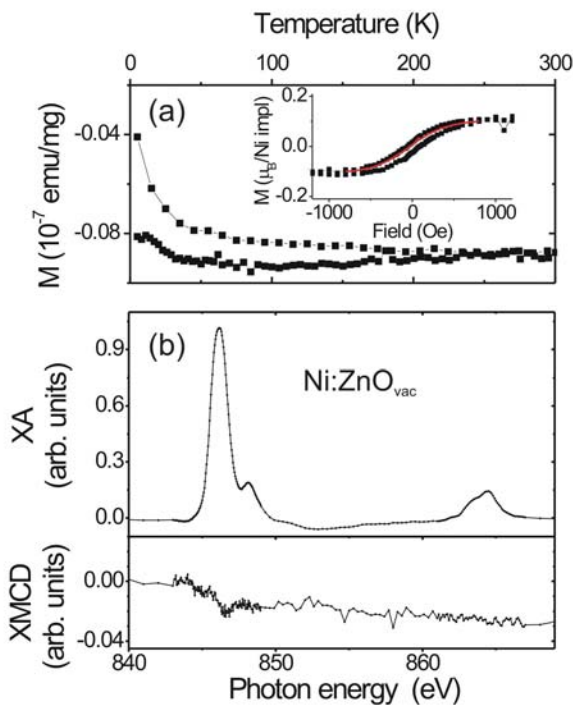


Fig. 5. (a) ZFC/FC at 50 Oe and magnetization reversal loops (insets) at 5 K (black) and 300 K (red) for XX:ZnO<sub>vac</sub> (a) and Ni:ZnO<sub>vac</sub> (b). The diamagnetic background has been

subtracted for the loops. The 300 K loop was measured partially. (b) XMCD for Ni:ZnO<sub>vac</sub> measured 4 weeks after post annealing. The XA spectrum (upper part) compares to the one for Ni:ZnO<sub>vac</sub> from Fig. 1a. The XMCD signal does not show any significant ferromagnetism at the Ni ions.

## V. Discussion and Conclusion

In this part we discuss the possible origin of the nanoparticle suppression and the ferromagnetic signal observed for the post-annealed Ni:ZnO<sub>vac</sub>. The mechanism of suppression of nanoparticle formation can be connected to a large extent to the formation of mosaicity. Along with the preparation, mosaicity as well as tensile strain constantly increase in contrast to Ni:ZnO<sub>purch</sub>. This shows that the annealing behavior of the ZnO lattice depends on its initial degree of destruction<sup>22</sup>. The increased number of grain boundaries might act as sinks for the implanted Ni ions. Thus, high TM solubility in ZnO can just originate from trapping by grain boundaries and might not originate from incorporation of TM ions into regular lattice sites. If, however, a sizeable amount of Ni is incorporated into the ZnO lattice, our pre-annealing approach leads to immobilization of excess TM ions in magnetically inactive agglomerates that do not provide a ferromagnetic signal which can be confused with DMS formation.

In order to check, if the trapping and immobilization of the Ni monomers takes place during the post-annealing procedure or occurs already at “room temperature” after implantation, we performed post annealing of a part of the as-implanted Ni:ZnO<sub>purch</sub> 4 months after implantation. As shown in Fig. 6, magnetometry revealed much lower  $T_{\max}$  and saturation magnetization as for Ni:ZnO<sub>purch</sub> annealed immediately after implantation

(Fig. 4a). Thus we conclude that such long waiting time at “room temperature” allows the small amount of grain boundaries present in the as-implanted Ni:ZnO<sub>purch</sub> to trap Ni ions and to prevent nanoparticle formation due to post annealing.

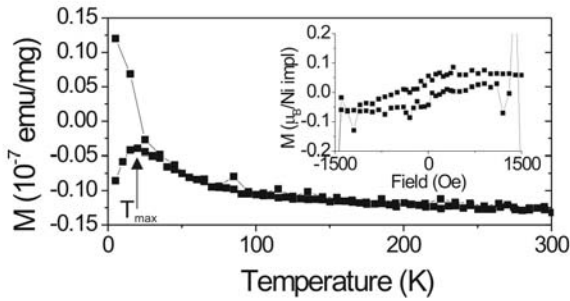


Fig. 6. ZFC/FC temperature and magnetization-field dependence recorded at 5 K for Ni:ZnO<sub>purch</sub> annealed 4 months after implantation.

In the introduction we listed several possibilities to be the origin of ferromagnetic properties of TM doped semiconductors like ZnO, i.e. DMS, GMM, and superparamagnetic secondary phases. Ordinary superparamagnetic nanoparticles are found in the as-purchased crystal after implantation and mild post-annealing. There is no evidence for additional contributions to the ferromagnetic signal although a substantial amount of the implanted Ni ions is still dispersed after post annealing. The defect structure improves after post-annealing. On the other hand, Ni ions of vacuum annealed crystals are still completely dispersed after post-annealing. About a real chemical effect of the Ni ions on the observed ferromagnetic properties of Ni:ZnO<sub>vac</sub> it can only be speculated at that point. Degradation behavior and temperature independent hysteresis loops indicate the presence of defect induced GMM that would agree with the small ferromagnetic signal observed for XX:ZnO<sub>vac</sub> which also shows lower amounts of

defects. If the signals observed from  $XX:ZnO_{vac}$  and  $Ni:ZnO_{vac}$  are not correlated with each other, the fastly degrading ferromagnetism of the post-annealed  $Ni:ZnO_{vac}$  would be induced by the Ni itself. In such case, also the formation of metastable Ni based nanoparticles with high magnetic moments or indirect coupling of Ni ions can be the origin of the observed ferromagnetism for post-annealed  $Ni:ZnO_{vac}$ .

In conclusion we showed that Ni can be incorporated into single crystals at an atomic concentration of 5% by means of ion implantation and post-annealing. Secondary phase formation is prevented by vacuum pre-annealing. We observed weak ferromagnetic properties for the pre-annealed crystals that do not originate from ordinary superparamagnetic nanoparticles. These properties drastically degrade after 3 days. Such behavior might lead to puzzling results if different analysis methods separated by longer time periods are used.

The Advanced Light Source is supported by the Director, Office of Science, Office of Basic Energy Sciences, of the U.S. Department of Energy under Contract No. DE-AC02-05CH11231.

- 1 S. A. Wolf, D. D. Awschalom, R. A. Buhrman, J. M. Daughton, S. von Molnár, M. L. Roukes, A. Y. Chtchelkanova, und D. M. Treger, *Science* **294**, 1488 (2001).
- 2 T. Dietl, H. Ohno, F. Matsukura, J. Cibert, und D. Ferrand, *Science* **287**, 1019 (2000).
- 3 J. M. D. Coey, M. Venkatesan, und C. B. Fitzgerald, *Nat. Mater.* **4**, 173 (2005).
- 4 K. R. Kittilstved, W. K. Liu, D. R. Gamelin, *Nat. Mater.* **5**, 291 (2006).
- 5 K. Potzger, et al., *Appl. Phys. Lett.* **88**, 052508 (2006).

- 6 Shengqiang Zhou, K. Potzger, H. Reuther, G. Talut, F. Eichhorn, J. von Borany, W. Skorupa, M. Helm, and J. Fassbender, *J. Phys. D Appl. Phys.* **40**, 964 (2007).
- 7 Shengqiang Zhou, K. Potzger, J. von. Borany, R. Groetzschel, W. Skorupa, M. Helm, and J. Fassbender, to be published (2007).
- 8 Anna Zukova, Arunas Teiserskis, Sebastiaan van Dijken, Y. K. Gunko, and V. Kazlauskienė, *Appl. Phys. Lett.* **89**, 232503 (2006).
- 9 H. Beckmann and G. Bergmann, *Phys. Rev. Lett.* **83**, 2417 (1999).
- 10 M. Gruyters and D. Riegel, *Phys. Rev. Lett. (C)*, 1582 (2000).
- 11 Q. Wang, Q. Sun, B. K. Rao, P. Jena, and Y. Kawazoe, *J. Chem. Phys.* **119**, 7124 (2003).
- 12 L. S. Dorneles, M. Venkatesan, M. Moliner, J. G. Lunney, and J. M. D. Coey, *Appl. Phys. Lett.* **85**, 6377 (2004).
- 13 A. Hernando, P. Crespo, and M. A. García, *Phys. Rev. Lett.* **96**, 057206 (2006).
- 14 S. R. Shinde, S. B. Ogale, J. S. Higgins, H. Zheng, A. J. Millis, V. N. Kulkarni, R. Ramesh, R. L. Greene, and T. Venkatesan, *Phys. Rev. Lett.* **92**, 166601 (2004).
- 15 David W. Abraham, Martin M. Frank, and Supratik Guha, *Appl. Phys. Lett.* **87**, 252502 (2005).
- 16 K. Potzger, Shengqiang Zhou, H. Reuther, K. Kuepper, G. Talut, M. Helm, J. Fassbender, and J. D. Denlinger, *Appl. Phys. Lett.* **91**, 062107 (2007).
- 17 X. Q. Wei, B. Y. Man, M. Liu, C. S. Xue, H. Z. Zhuang, and C. Yang, *Physica B* **388**, 145 (2007).
- 18 S. J. Pearton, D. P. Norton, K. Ip, Y. W. Heo, and T. Steiner, *J. Vac. Sci. Technol. B* **22**, 932 (2004)

- 19 Ü. Özgür, Ya. I. Alivov, C. Liu, A. Teke, M. A. Reshchikov, S. Doğan, V. Avrutin, S.-J. Cho, and H. Morkoç, *J. Appl. Phys.* **98**, 041301 (2005).
- 20 K. Potzger, S. Q. Zhou, F. Eichhorn, M. Helm, W. Skorupa, A. Mücklich, J. Fassbender, T. Herrmannsdorfer, and A. Bianchi, *J. Appl. Phys.* **99**, 063906 (2006).
- 21 M. Finazzi, N. B. Brookes, F. M. F. de Groot, *Phys. Rev. B* **59**, 9933 (1999).
- 22 V. A. Coleman, H. H. Tan, C. Jagadish, S. O. Kucheyev, and J. Zou, *Appl. Phys. Lett.* **87**, 231912 (2005).
- 23 B. D. Cullity, *Elements of X-Ray Diffraction* (Addison-Wesley Reading, MA, 1978), p. 102.
- 24 A. I. Nesvizhskii, A. L. Andukinov, J. j. Reht, and K. Baberschke, *Phys. Rev. B* **62**, 15295 (2000).